Deformation associated with ghost craters and basins in volcanic smooth plains on Mercury: Strain analysis and implications for plains evolution

Christian Klimczak,[1] Thomas R. Watters,[2] Carolyn M. Ernst,[3] Andrew M. Freed,[4] Paul K. Byrne,[1] Sean C. Solomon,[1,5] David M. Blair,[4] and James W. Head[6]

Received 6 April 2012; revised 5 July 2012; accepted 5 July 2012; published 11 September 2012.

[1] Since its insertion into orbit about Mercury in March 2011, the MESSENGER spacecraft has imaged most previously unseen regions of the planet in unprecedented detail, revealing extensive regions of contiguous smooth plains at high northern latitudes and surrounding the Caloris basin. These smooth plains, thought to be emplaced by flood volcanism, are populated with several hundred ghost craters and basins, nearly to completely buried impact features having rims for which the surface expressions are now primarily rings of deformational landforms. Associated with some ghost craters are interior groups of graben displaying mostly polygonal patterns. The origin of these graben is not yet fully understood, but comparison with numerical models suggests that the majority of such features are the result of stresses from local thermal contraction. In this paper, we highlight a previously unreported category of ghost craters, quantify extensional strains across graben-bearing ghost craters, and make use of graben geometries to gain insights into the subsurface geology of smooth plains areas. In particular, the style and mechanisms of graben development imply that flooding of impact craters and basins led to substantial pooling of lavas, to thicknesses of ~1.5 km. In addition, surface strains derived from groups of graben are generally in agreement with theoretically and numerically derived strains for thermal contraction.

Citation: Klimczak, C., T. R. Watters, C. M. Ernst, A. M. Freed, P. K. Byrne, S. C. Solomon, D. M. Blair, and J. W. Head (2012), Deformation associated with ghost craters and basins in volcanic smooth plains on Mercury: Strain analysis and implications for plains evolution, *J. Geophys. Res.*, *117*, E00L03, doi:10.1029/2012JE004100.

1. Introduction

[2] Surface deformation on Mercury is dominated by thrust faulting, expressed either by lobate scarps that are typically several hundred kilometers in length, or by smaller-scale wrinkle ridges that occur primarily in areas of volcanic smooth plains [e.g., *Strom et al.*, 1975]. The predominance of contractional structures is widely believed to reflect a thermal history dominated by interior cooling and global contraction [e.g., *Solomon*, 1977; *Solomon et al.*, 2008]. From images acquired during the flybys of Mercury by the Mariner 10 and MErcury Surface, Space ENvironment, GEochemistry, and Ranging (MESSENGER) spacecraft, extensional structures were observed only on plains within large- and medium-scale impact basins (Figure 1), such as the Caloris [e.g., *Strom et al.*, 1975; *Melosh and McKinnon*, 1988; *Solomon et al.*, 2008; *Murchie et al.*, 2008; *Watters et al.*, 2009a], Rembrandt [*Watters et al.*, 2009b], and Raditladi and Rachmaninoff [*Solomon et al.*, 2008; *Watters et al.*, 2009c; *Prockter et al.*, 2010] basins. However, orbital data from MESSENGER revealed several groups of troughs on smooth plains (Figure 1) well outside of large basins [*Head et al.*, 2011; *Watters et al.*, 2012].

[3] In addition to the large expanses of smooth plains within major impact basins [e.g., *Strom et al.*, 1975; *Spudis and Guest*, 1988], smooth plains surround the Caloris basin [e.g., *Strom et al.*, 1975; *Spudis and Guest*, 1988; *Fassett et al.*, 2009; *Head et al.*, 2009] and are found at high northern latitudes [*Head et al.*, 2011]. The circum-Caloris smooth plains [*Fassett et al.*, 2009; *Head et al.*, 2009] and the smooth plains at high northern latitudes [*Head et al.*, 2011] are

[1]Department of Terrestrial Magnetism, Carnegie Institution of Washington, Washington, D. C., USA.
[2]Center for Earth and Planetary Studies, National Air and Space Museum, Smithsonian Institution, Washington, D. C., USA.
[3]Johns Hopkins University Applied Physics Laboratory, Laurel, Maryland, USA.
[4]Department of Earth and Atmospheric Sciences, Purdue University, West Lafayette, Indiana, USA.
[5]Lamont-Doherty Earth Observatory, Columbia University, Palisades, New York, USA.
[6]Department of Geological Sciences, Brown University, Providence, Rhode Island, USA.

Corresponding author: C. Klimczak, Department of Terrestrial Magnetism, Carnegie Institution of Washington, Washington, DC 20015, USA. (cklimczak@ciw.edu)

0148-0227/12/2012JE004100

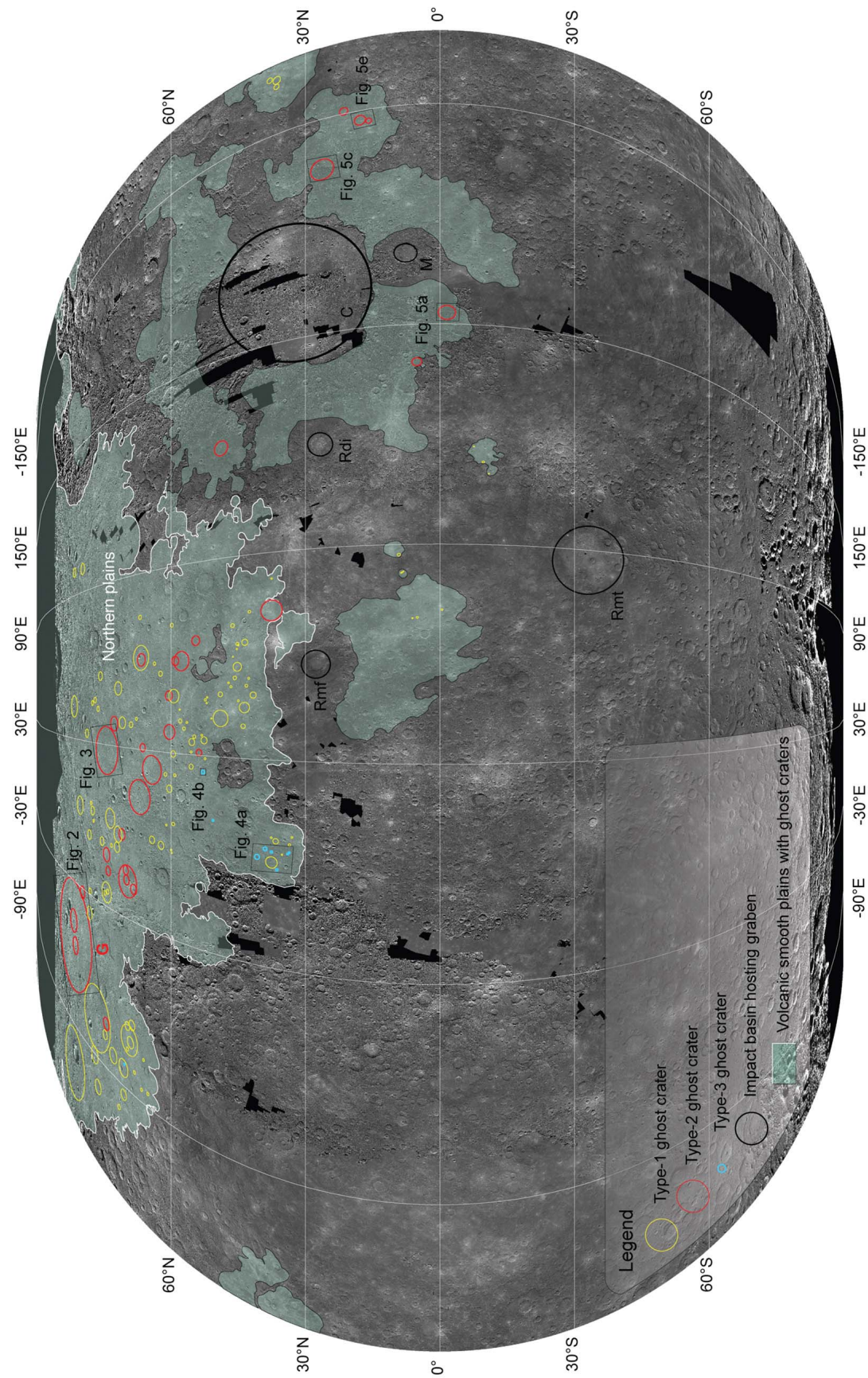

Figure 1. Global distribution of the three types of ghost craters on volcanic smooth plains on Mercury, shown on MESSENGER's MDIS monochrome base map (~250 m/pixel resolution) in a Winkel II projection centered at 45°E longitude. The northern plains are outlined in white. Also shown are large impact basins with graben in the basin interior: C: Caloris basin; M: Mozart basin; Rmf: Rachmaninoff basin; Rdi: Raditladi basin; Rmt: Rembrandt basin. The base map is available at http://messenger.jhuapl.edu/the_mission/mosaics.html.

temporally unrelated to nearby large impact structures and are interpreted to be of volcanic origin. Flood volcanism, therefore, is regarded as the primary mechanism for plains unit emplacement, burying cratered terrain under thick layers of lava [*Head et al.*, 2011]. Subsequent contractional deformation is manifested by widespread wrinkle ridges across these plains.

[4] Assemblages of troughs, interpreted to be graben, occur in these smooth plains together with wrinkle ridges. These two types of tectonic features display complex crosscutting relationships [*Watters et al.*, 2012]. Many of the sets of graben are interior to "ghost" craters and basins, impact features that have been buried by volcanic flows and are visible at present only by a ring-shaped set of deformational structures thought to overlie the buried crater rim [e.g., *Head et al.*, 2008; *Watters et al.*, 2009a]. *Watters et al.* [2012] described the diversity of these assemblages of extensional and contractional landforms, which range from individual crater-sized systems (<50 km in diameter) to much larger systems associated with buried basins (>300 km in diameter), some of which host ghost craters in their interiors.

[5] These graben–wrinkle ridge assemblages have been postulated to be the result of some combination of subsurface drainage, cooling, vertical motions, and larger-scale deformation [*Head et al.*, 2011]. Crosscutting and superposition relationships of graben and wrinkle ridges suggest that extension generally predated the most recent episode of contraction, though wrinkle ridge development may have initiated in some areas prior to the formation of the graben [*Watters et al.*, 2012]. From these observations, *Watters et al.* [2012] proposed that graben formed as a result of cooling and thermal contraction of the uppermost volcanic unit. Thermomechanical simulations have shown that, under specific circumstances, cooling of a thick layer of volcanic material can cause extensional stresses of sufficient magnitude to form graben [*Watters et al.*, 2012; A. M. Freed, et al., On the origin of graben and ridges at buried basins in Mercury's northern plains, submitted to *Journal of Geophysical Research*, 2012]. By this interpretation, wrinkle ridges continued to be active over much longer timescales, durations consistent with a strong influence from the global cooling and contraction of the planetary interior.

[6] In this paper, we describe the several types of ghost craters, analyze the groups of graben located within many such features in terms of the accommodated extensional strain, and explore how measured strains correlate with those predicted by thermal contraction and modeled in thermomechanical simulations (Freed et al., submitted manuscript, 2012) for a variety of rock types, temperature ranges, and layer thicknesses. Combining these results with observed graben geometries, we then interpret the subsurface geological units and explore implications for the geologic evolution of volcanic smooth plains on Mercury.

2. Characteristics of Ghost Craters

[7] Ghost craters have been documented on volcanic plains units on Mars and the Moon [e.g., *Strom*, 1971; *Cruikshank et al.*, 1973; *Brennan*, 1975; *Hartmann and Esquerdo*, 1999], and may exist on Venus. Such features are particularly well developed on the major smooth plains units of Mercury. We have mapped more than 200 ghost craters and basins with complete or nearly complete rings of wrinkle ridges on Mercury (Figure 1). A majority are located in Mercury's northern smooth plains.

2.1. Ghost Craters in the Northern Volcanic Plains

[8] On the northern smooth plains, wrinkle-ridge rings outline impact features as small as craters 10–20 km in diameter and as large as basins several hundred kilometers in diameter, such as the 300-km-diameter Goethe basin (Figure 2). Two types of ghost craters dominate the population of such features on Mercury. Type-1 ghost craters consist only of a wrinkle-ridge ring [e.g., *Head et al.*, 2011, Figure 4a]. Type-2 ghost craters are outlined by circular wrinkle ridges and contain graben in their interiors (Figures 2 and 3). The type-2 ghost crater population has a higher proportion of large craters and basins than the type-1 group and includes no ghost craters smaller than 40 km in diameter. Both type-1 and type-2 ghost craters occur generally well inward of the boundaries of the northern plains (Figure 1). Type-2 craters frequently occur next to those of type 1, with no obvious preferred clustering of either type, thus posing a challenge to explanations for the formation of these landforms with a single, consistent tectonic model [*Watters et al.*, 2012].

[9] A total of 25 type-2 ghost craters have been mapped to date in the northern smooth plains. Of these, 16 contain, or are contained within, other type-1 or type-2 ghost craters, whereas nine are found as individual features (Figure 1). Wrinkle ridges that encircle type-2 ghost craters in the northern smooth plains form complete rings in all cases, and topographic profiles derived from MESSENGER's Mercury Laser Altimeter (MLA) [*Cavanaugh et al.*, 2007] show that such rings stand up to 500 m above the surrounding plains units and that the crater floors lie between 400 and 600 m below the peak elevation of the ridge rings (Figures 2b and 3c). Graben within type-2 ghost craters form broadly polygonal patterns (Figures 2a, 2c, 3a, and 3b), but preferred radial and circumferential orientations have been documented for the two ghost craters contained inside the Goethe basin (Figure 2a) and in ghost craters within similar basins in the northern plains [*Watters et al.*, 2012]. Typically, the circumferentially oriented graben are found to be localized near, or are superposed on, the wrinkle-ridge rings [*Watters et al.*, 2012].

[10] Graben are found throughout the interiors of type-2 ghost craters and basins, but there is generally a higher density of such features toward the crater centers (see map in auxiliary material).[1] Graben are typically 5 to 10 km long and up to 1 ± 0.2 km wide (Figures 2c, 2d, 2e, 2f, and 3b). Some of the longest and widest graben are seen in the two ghost craters interior to Goethe basin, reaching widths of 1.2 to ~1.8 km and lengths in excess of 20 km [*Watters et al.*, 2012]. Different stages of graben development may also be inferred. Some graben are isolated, do not show evidence of having interacted with other graben (e.g., fault linkage), and display a typical continuous deepening of the graben floor toward the graben center (Figure 2e). Others are segmented (Figure 2d) or linked (Figure 2f). The majority

[1] Auxiliary materials are available in the HTML. doi:10.1029/2012JE004100.

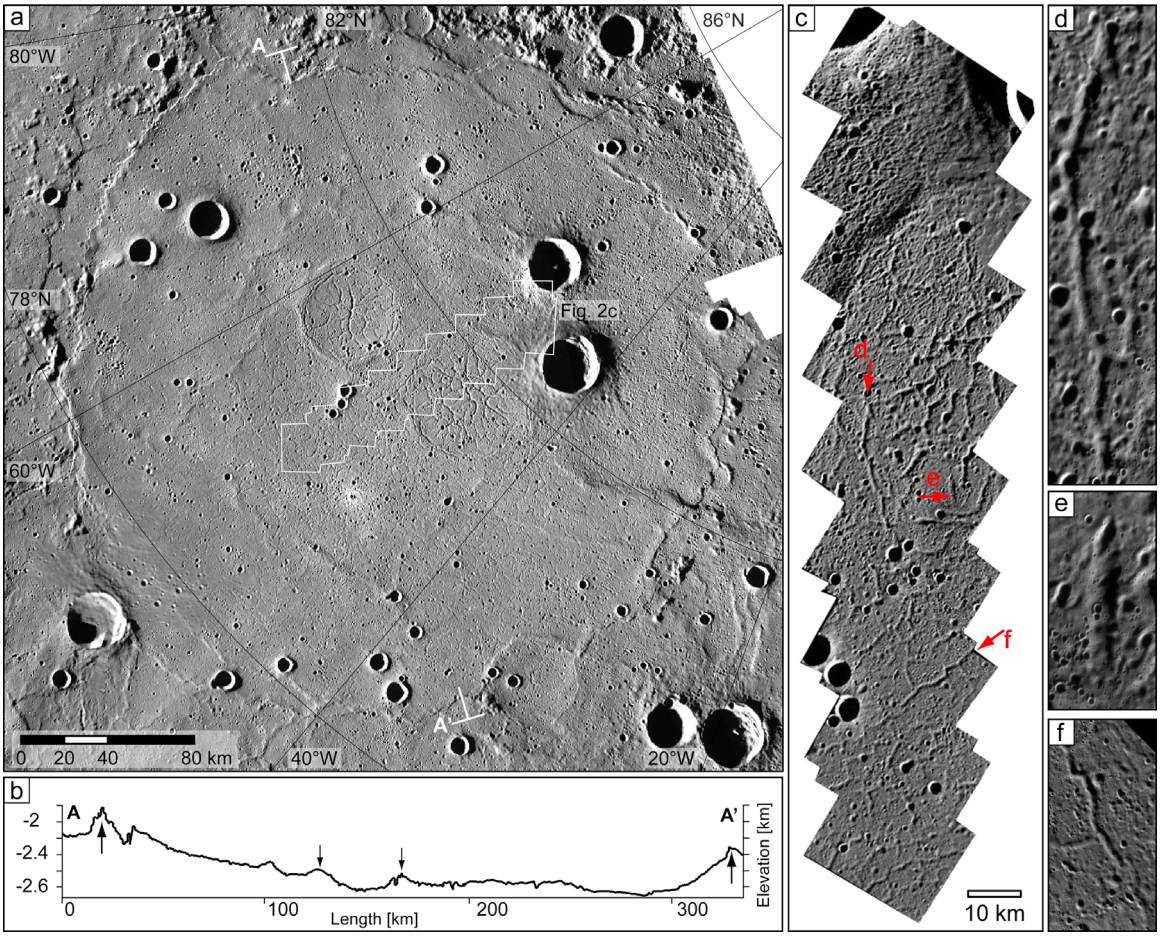

Figure 2. Fractures in smooth plains material within the Goethe basin. (a) Overview of Goethe basin and interior ghost craters. Fracturing is most pronounced within two ghost craters in the center of the basin. Map is a close-up from the MDIS monochrome base map in polar stereographic projection centered at the north pole. (b) Topographic profile obtained from MLA gridded topography along the transect A–A′ in Figure 2a. The elevated topography of the wrinkle-ridge ring above the buried basin rim (large arrows) and the wrinkle-ridge ring above the rim of one of the interior ghost craters (small arrows) are evident. Note the overall tilt of the surface of the smooth plains on the basin floor toward A′. (c) High-resolution target mosaic of central Goethe basin and a portion of a basin-interior ghost crater. Locations of features in Figures 2d–2f are indicated. From images EN0223614570M, EN0223614576M, EN0223614582M, EN0223614588M, EN0223614594M, EN0223614600M, EN0223614606M, EN0223614612M, EN0223614618M, EN0223571371M, EN0223571377M, EN0223571383M, EN0223571389M, EN0223571395M, EN0223571401M, EN0223571407M, EN0223571413M, and EN0223571419M. (d) Detailed image of a segmented graben. (e) Typical individual graben, showing a continuous decrease in the elevation of the graben floor toward the graben center. (f) Graben of differing orientations after they have been linked into one coalesced structure.

of graben have fairly constant widths along their lengths and show more or less constant shadow widths (e.g., Figures 2d, 2f, and 3b). This geometry suggests that graben floors did not accumulate maximum displacements in the center of the structure but rather show an approximately constant displacement along their lengths, implying that graben development and normal fault growth were restricted (e.g., confined to a mechanical layer of limited thickness) [e.g., *Nicol et al.*, 1996; *Soliva and Benedicto*, 2005; *Soliva et al.*, 2006; *Polit et al.*, 2009] within the majority of type-2 ghost craters. However, even high-resolution images (~20 m/pixel) obtained with MESSENGER's Mercury Dual Imaging System (MDIS) [*Hawkins et al.*, 2007] do not allow sufficiently precise shadow measurements for the construction of displacement profiles to detect fault restriction unequivocally, given that fault throws even for the widest graben in Goethe basin inferred from MLA profiles exceed the image resolution by a factor of only 3–4.

[11] A third, previously unreported type of ghost crater is present in the northern smooth plains. For this class of ghost crater, which includes nine examples as of this writing, wrinkle-ridge rings are not prominent or are missing. Instead, a graben ring demarks the outline of the buried crater (Figure 4). Type-3 ghost craters range from 10 to ~50 km in diameter and tend to occur closer to the edges of the northern smooth plains unit than the other types. There is a cluster at

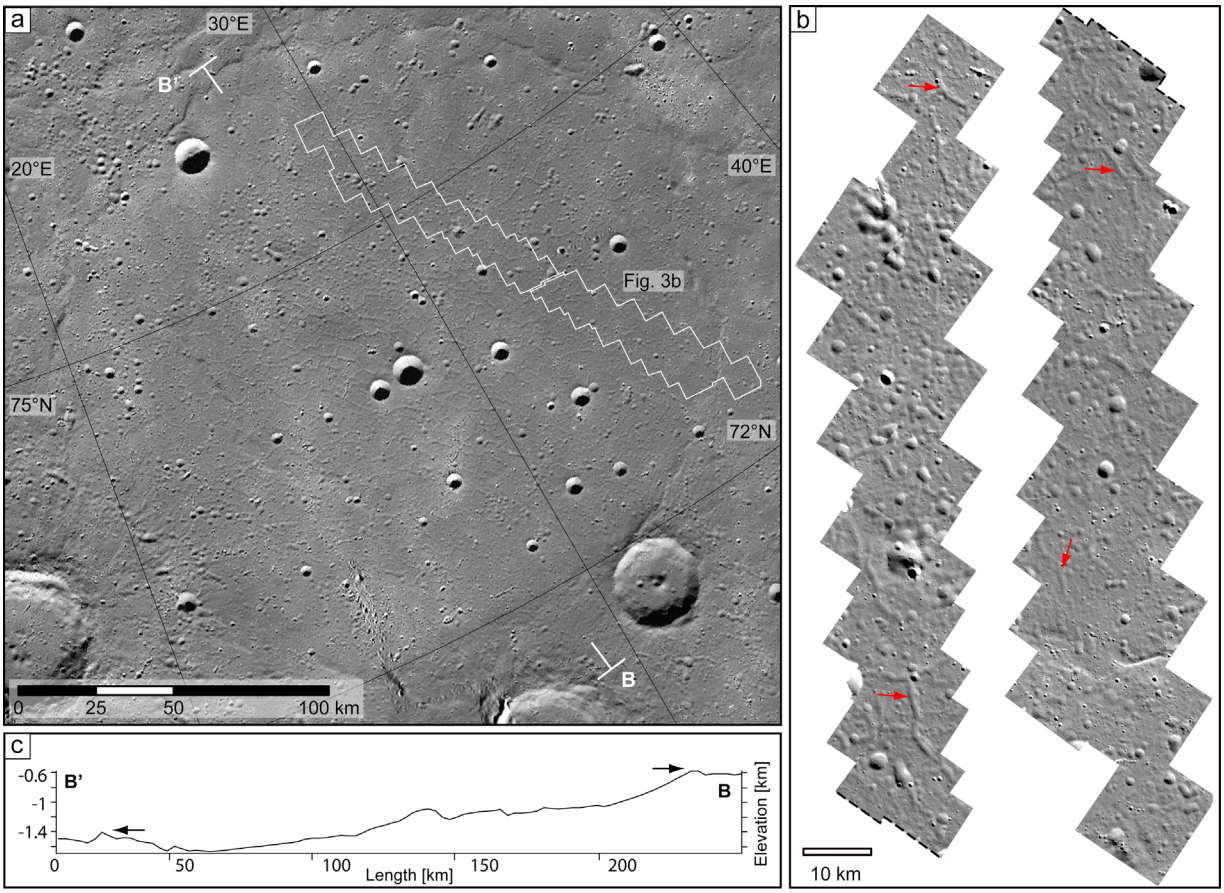

Figure 3. Fractures in smooth plains that partially fill a 200-km-diameter basin. (a) Overview of the basin and interior graben from the MDIS monochrome base map in polar stereographic projection centered at the north pole. (b) Mosaic of targeted high-resolution images (EN0221929759M, EN0221929762M, EN0221929765M, EN0221929768M, EN0221929771M, EN0221929774M, EN0221929777M, EN0221929780M, EN0221929783M, EN0221929786M, EN0222016201M, EN0222016204M, EN0222016207M, EN0222016210M, EN0222016213M, EN0222016216M, EN0222016219M, and EN0222016222M) of a portion of the basin showing subtle expressions of graben (arrows). (c) Topographic profile along the transect B–B′ in Figure 3a. The elevated topography of the wrinkle-ridge ring that marks the buried basin rim is indicated by arrows. Note the overall tilt of the smooth plains surface on the basin floor toward B′.

0°E longitude (Figure 4a), and a few individual examples can be seen south of the Goethe basin (Figure 1). The graben forming these rings are ~1 km wide (Figure 4b), and there are no graben within the ghost crater interior. For some type-3 ghost craters, a portion of the original crater rim is exposed, indicative of thinner volcanic fill in the areas of these structures. A possible formation mechanism for graben rings on Mercury has been discussed by Freed et al. (submitted manuscript, 2012), and a similar mechanism for forming graben rings on Mars was offered earlier by *Buczkowski and Cooke* [2004].

2.2. Ghost Craters in Smooth Plains Exterior to Caloris

[12] The smooth plains unit exterior to the Caloris impact basin, a unit that generally coincides with the mapped extent of the Odin Formation [*Fassett et al.*, 2009], also hosts type-1 and type-2 ghost craters (Figure 1), but such features are fewer and less diverse than in the northern plains. Their distributions also differ. Type-1 ghost craters occur to the east of Caloris but type-2 features do not, whereas to the south and northwest of the Caloris basin type-2 ghost craters are found but fully developed type-1 ghost craters are not. We have identified seven type-2 ghost craters in this region (Figure 1).

[13] For type-2 ghost craters in the Caloris exterior plains, wrinkle-ridge rings typically only partially encircle the buried craters, and part of the original crater or basin rim is still exposed (Figure 5c). Some ghost craters have no wrinkle-ridge ring at all but only more rugged plains above the inferred crater rim (Figure 5e, southern crater). Both types of relationships are indicative of thinner volcanic fill than in areas where ghost craters of comparable diameter are marked by fully developed wrinkle-ridge rings. In these ghost craters, graben occur in clusters that are concentrated in some parts of the crater or basin, whereas other parts are devoid of graben and are instead deformed by features indicative of shortening (Figure 5a and 5c). Individual graben are 5 to 10 km long and are usually less than 1 km in width (Figure 5b, 5d, and 5f). In contrast to the polygonal graben patterns seen within ghost craters in the northern

smooth plains, graben in the Caloris exterior plains tend to have circular patterns (see arrows in Figures 5b, 5d, and 5f) broadly similar to those in type-3 ghost craters.

2.3. Comparison With Ghost Craters on the Moon and Mars

[14] Ghost craters are found on Mars and the Moon in geologic settings similar to those described here. On the Moon, ghost craters are seen where mare basaltic lava flows are thought to have partially flooded pre-existing craters [*Cruikshank et al.*, 1973; *Brennan*, 1975; *Schultz*, 1976]. Some lunar ghost craters have muted rims, whereas others show "ring composite structures" consisting of either remnants of the original crater rim or circumferential wrinkle ridges localized above the buried rim. Many lunar ghost craters are only a few kilometers in diameter [*Cruikshank et al.*, 1973], smaller than the average-size ghost craters observed on Mercury, but ghost craters with diameters of 50 km or more are seen, such as the ~57-km-diameter Lambert R crater [*Brennan*, 1975, Figure 2b]. All lunar ghost craters fit the characteristics of type-1 features. Neither type-2 nor type-3 ghost craters are apparent on the Moon, although volcanically and tectonically modified lunar craters can contain fractures and graben; such features are termed floor-fractured craters [*Schultz*, 1976].

[15] Large type-1 ghost craters with near-perfect rings of wrinkle ridges are found in ridged plains volcanic units throughout Mars, particularly in Hesperia Planum [e.g., *Watters*, 1993, Figure 6]. In the northern lowlands of Mars, *Frey et al.* [2002] identified hundreds of topographic patterns they called quasi-circular depressions, which they interpreted to be the surface expression of buried impact craters [*Frey et al.*, 2002; *Buczkowski et al.*, 2005]. *Hartmann and Esquerdo* [1999] described small (1.2 to 2.1 km diameter) "pathologically deformed" impact craters on Mars, and they attributed such features to volcanic burial, interactions with ice, or viscous relaxation of relief.

[16] Areas in which graben display multiple orientations and outline polygonal shapes similar to the polygonal terrain in type-2 ghost craters on Mercury are ubiquitous in volcanic plains units on Venus [e.g., *Smrekar et al.*, 2002] and across the Martian northern lowlands, where they are termed either patterned ground [*Mangold*, 2005] or labyrinthi. At one location in Chryse Planitia on Mars, such labyrinthi formed within a 120-km-diameter ghost crater with a partially exposed rim (Figure 6), similar to type-2 ghost craters in the Caloris exterior plains (e.g., Figure 5c). Graben within that Martian ghost crater are oriented so as to form polygons (Figure 6a), whereas graben outside the crater have circular patterns (Figure 6b). It is unclear whether the graben inside the Martian ghost crater formed under the same circumstances as those that led to the similar-appearing ghost craters on Mercury, because the geological settings and near-surface materials may both differ. Numerical modeling of strain in areas of similar graben in Utopia Planitia indicated consistency with formation by contraction of wet sediments over pre-existing topographic highs [*Buczkowski and Cooke*, 2004; *Cooke et al.*, 2011], such as where graben rings, similar to those found at type-3 ghost craters on Mercury,

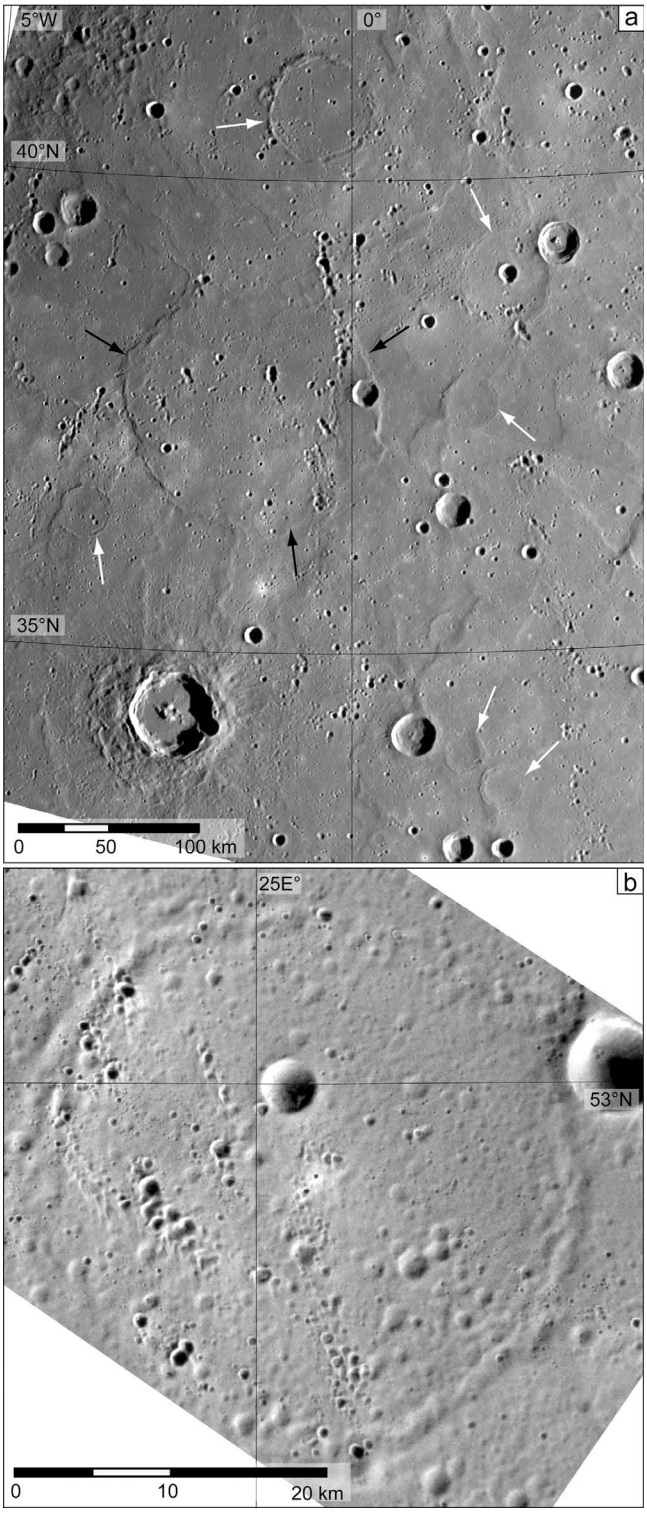

Figure 4. Type-3 ghost craters defined by a graben ring. (a) Graben rings and partial graben rings in smooth plains material mark the rims of buried craters (white arrows). A larger type-1 ghost crater marked by a wrinkle-ridge ring is indicated by black arrows. Mosaic from the MDIS monochrome base map in polar stereographic projection centered at the north pole. (b) Targeted high-resolution image (EN0220546642M) of a type-3 ghost crater with its graben ring. No wrinkle ridges or other graben are associated with this ghost crater. Image in equirectangular projection.

form over a buried crater rim [*Buczkowski and Cooke*, 2004].

3. Strain Analysis

3.1. Extensional Strain Across Type-2 Ghost Craters

[17] Quantifying the extensional strain accommodated by graben on a planetary surface, such as those found in ghost craters on Mercury, can provide insight into the tectonic processes responsible for the deformation [e.g., *Klimczak et al.*, 2010]. Moreover, characterizing variations in the distribution of strain across a faulted region can illuminate the geologic and structural development of the area. *Watters et al.* [2012] and Freed et al. (submitted manuscript, 2012) discussed and modeled a variety of proposed mechanisms for the formation and evolution of type-2 ghost craters (those

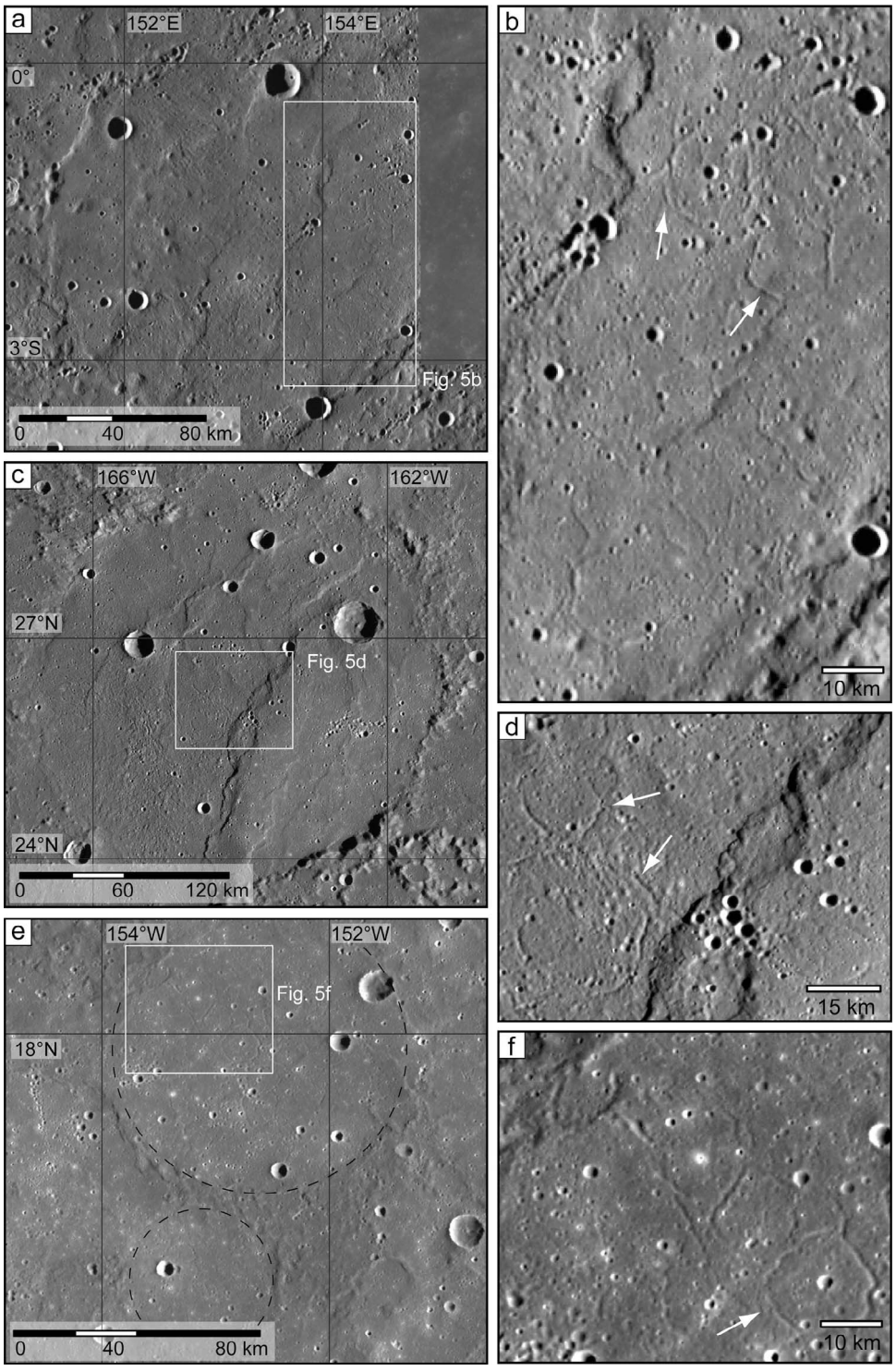

Figure 5

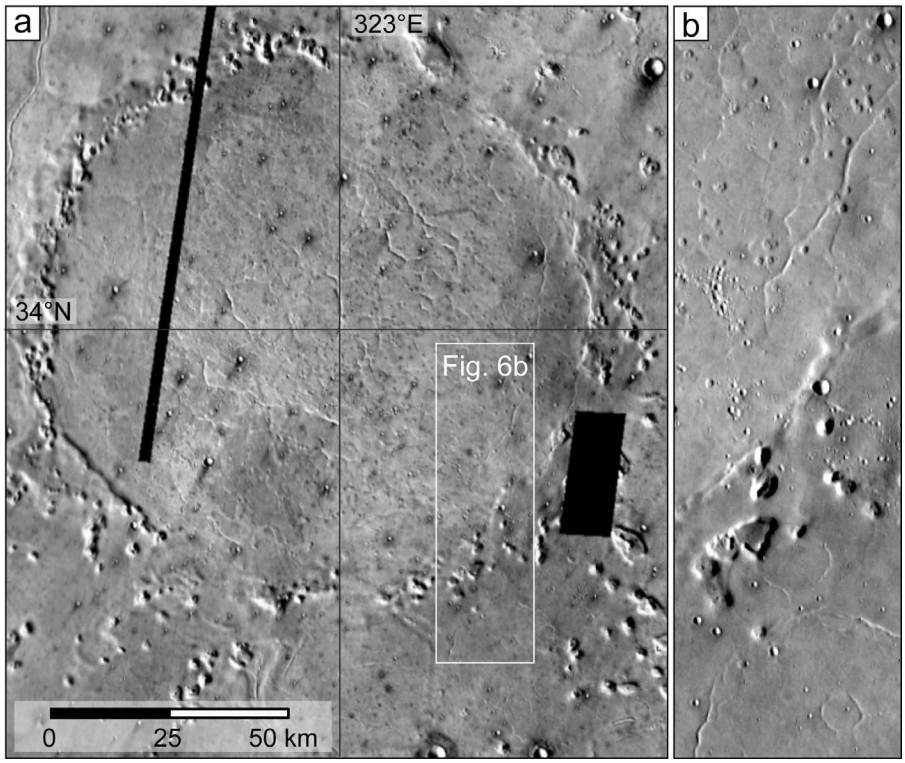

Figure 6. Infrared images from the Thermal Emission Imaging System (THEMIS) on the Mars Odyssey spacecraft of an unnamed ghost crater in Chryse Planitia, Mars. (a) Ghost crater containing troughs that form large polygons. Mosaic from images I33809009, I10574009, I02398005, I10237008, I10237008, and I28769011 in equirectangular projection. (b) Close-up view (image I05007005) of the southeastern rim of the crater showing troughs inside and outside the crater with orientations similar to those of graben in ghost craters on Mercury.

with systems of graben and wrinkle ridges) on Mercury, including isostatic uplift, lower crustal flow, volcanic loading, and a combination of global contraction from interior cooling and local thermal contraction from cooling of lava flow units. Both sets of workers reached the conclusion that graben in type-2 ghost craters likely formed as a result of thermal contraction of thick layers of flood lavas. In the models of those studies, the thermal contraction of the cooling lavas produced extensional deformation as a result of resistive forces exerted on the contracting material by the underlying, non-contracting units.

[18] Here, we provide measurements of the longitudinal extensional strain across type-2 ghost craters, derived from the geometry of graben imaged within the craters. We have analyzed the magnitude and distribution of strain across each region and compared the strains with those predicted by models for thermal contraction for a variety of possible rock types. To better characterize the geologic evolution and deformation of smooth plains, we have also made use of the thermomechanical numerical models of Freed et al. (submitted manuscript, 2012) to investigate controls on the amount of strain in these plains by testing the model's sensitivity to temperature change, thickness of the volcanic cover, coefficient of thermal expansion, and degree to which underlying material provides resistance to contraction of the youngest major cooling unit.

[19] A simple measure of the average longitudinal extensional strain (ε_1), the strain measured along a linear traverse,

Figure 5. Type-2 ghost craters in smooth plains exterior to the Caloris basin. (a) A wrinkle-ridge ring surrounds a volcanically buried ~150-km-diameter basin south of Caloris. Multiple approximately north–south-oriented wrinkle ridges transect the buried basin. The plains in the eastern portion of the basin contain narrow graben, whereas the western half of the basin is characterized by knobs and hills typical of the Odin Formation. (b) Detailed view of the graben in the buried basin shown in Figure 5a. (c) Basin ~190 km in diameter partially filled with smooth plains. A partial wrinkle-ridge ring outlines a portion of the western basin rim. Several wrinkle ridges and a lobate scarp, both oriented northeast–southwest, transect the basin. Narrow graben are found in the basin center. (d) Detailed view of graben on the plains within the basin in Figure 5c. These graben have circular orientations (arrows). (e) Two fully buried type-2 ghost craters of diameters ~90 and ~50 km (dashed circles). Note the relatively rugged terrain between the ghost craters, which helps to demarcate the shallowly buried crater rims. Wrinkle ridges only partially outline the northern ghost crater, whereas the southern ghost crater lacks a ridge ring. (f) Detailed view of graben on the smooth plains within the northern ghost crater in Figure 5e. Some graben form quasi-circular patterns (arrow). All images are portions of the MDIS monochrome base map in equirectangular projection.

across type-2 ghost craters in the northern smooth plains may be derived from a surface areal strain analysis. If the troughs within such craters are regarded as opening-mode fractures, then the areal extensional strain, ε_a, is the ratio of the area occupied by troughs to the total area inside a ghost crater. The square root of the areal strain then yields the average longitudinal strain, a value that enables easy comparison with results for thermal contraction from both theoretical considerations and two-dimensional numerical modeling. If strain is more or less isotropic within the ghost craters, the conversion from areal to longitudinal extensional strain allows all troughs mapped in the ghost crater to contribute to the measured strain, independent of their orientations. This treatment yields a more general result than does the use of longitudinal strain measurements along individual profiles, which do not include the contributions of graben parallel to or not intersected by the profile.

[20] Of course, the troughs within type-2 ghost craters are not opening-mode fractures but rather are graben: linear depressions bordered by two antithetic normal faults, as inferred from high-resolution targeted images [*Watters et al.*, 2012]. The full width of the graben does not contribute to extension across the structure, therefore, and the longitudinal strains must be adjusted. The extension expressed by a graben can be measured in high-resolution images by determining the rim-to-rim width of the graben and the graben floor width. The difference between these width measurements equals the combined heaves of the two bounding normal faults and thus the total extension across the graben. Width measurements range from 400 to 600 m for graben floors, and from 800 to 1200 m for the distance between graben rims. Measurements on targeted images at resolutions of 30 to 40 m/pixel were taken to an accuracy of 1–2 pixels, so that uncertainties in the measurements are <100 m. For all the structures we examined, graben floors are consistently about half as wide as the distance between the graben rims. Thus the extensional strains expressed by the graben are ~50% of the longitudinal extensional strains obtained from the simple area analysis, obtained under the assumption that the troughs are opening-mode fractures.

[21] The adjusted longitudinal extensional strains across all type-2 ghost craters within the northern smooth plains are shown in Figure 7 in relation to MLA topography [*Zuber et al.*, 2012]. Measured strains, which are generally minimum estimates inasmuch as some strain might be unresolved in currently available images, range from $\varepsilon_l = 0.36\%$ up to $\varepsilon_l = 3.43\%$, but the great majority of strain values are between 1% and 1.5% (Figure 7). Strains at the lower end of measured values ($\varepsilon_l < 1\%$) are associated with ghost craters comparatively close to the edge of the northern smooth plains, whereas the higher strains ($\varepsilon_l > 1.5\%$) are associated with ghost craters contained within buried basins, such as the ghost craters inside Goethe basin, or are found in buried basins and craters in the central parts of the northern smooth plains (Figure 7). Notably, the central part of the northern smooth plains is marked by a rise of more than 1.5 km in topographic relief (Figure 7) [*Zuber et al.*, 2012]. On the flanks of the rise are several ghost craters. Extensional strains across such ghost craters that do not lie within larger buried impact structures are observed to be highest (Figure 7). Those ghost craters tilt away from the center of the rise (Figures 3c and 7).

[22] Because the formation of pervasive graben in ghost craters is best modeled as the result of thermal contraction of a thick layer of volcanic material [*Watters et al.*, 2012; Freed et al., submitted manuscript, 2012], measured longitudinal extensional strains across type-2 ghost craters should be in approximate agreement with longitudinal strains predicted for thermal contraction of rocks. The longitudinal strain for thermally contracted volcanic rock is the product of the coefficient of thermal expansion, α, of the appropriate rock type and the temperature change, ΔT, in the form:

$$\varepsilon_l = \frac{\Delta l}{l_0} = \alpha \cdot \Delta T, \tag{1}$$

where Δl denotes the change in length of a material along a linear traverse and l_0 is the original length of the material.

[23] The accumulation of thermal contractional strain in volcanic rocks starts when the temperature cools to the elastic blocking temperature of the rock, T_e, which can be as high as 800° to 900°C for basalts [*Turcotte*, 1983]. Average surface temperature T_0 in the northern plains can be as low as 0 to −100°C [*Vasavada et al.*, 1999]. At Mercury's hot poles (the equatorial regions at latitudes 0° and 180° that because of the planet's spin–orbit resonance and eccentric orbit, face the Sun at alternating perihelia), T_0 can be as high as 150°C [e.g., *Vasavada et al.*, 1999; *Williams et al.*, 2011]. The temperature change, ΔT, that contributes to thermal contractional strain is thus ~800 to 1000 K in the northern plains and as little as ~600 K in the plains units exterior to the Caloris basin. The longitudinal strain of thermal contraction should be $\varepsilon_l \sim 1.85\%$ for rocks of basaltic composition cooling by $\Delta T = 1000$ K at temperatures less than the elastic blocking temperature (Figure 8). Near the hot pole at the Caloris exterior plains, strains should be somewhat lower than in the colder northern plains and are not likely to exceed $\varepsilon_l \sim 1\%$ (Figure 8) for basaltic compositions.

[24] Elemental remote sensing observations by the MESSENGER X-Ray Spectrometer (XRS) indicate that the surface of Mercury has an average composition intermediate between that of iron-poor basalts and those of more ultramafic materials [*Nittler et al.*, 2011]. XRS spectra at the highest spatial resolution, obtained during energetic solar flares, indicate that the northern smooth plains have major element ratios consistent with a basalt-like composition, but the surrounding heavily cratered terrain has a generally more magnesian composition approaching that of terrestrial komatiites [*Weider et al.*, 2012]. Experimentally determined linear coefficients of thermal expansion for terrestrial and lunar rocks of basaltic composition range from $\alpha \approx 10^{-5}$ K^{-1} for lunar impact melt [*Richter and Simmons*, 1974] and olivine [*Singh and Simmons*, 1976], a major component of mafic rocks, to $\alpha \approx 2.6 \times 10^{-5}$ K^{-1} for gabbros [*Richter and Simmons*, 1974].

[25] The iron content of the volcanic plains units on Mercury is lower than that of the measured rock types for coefficients of thermal expansion given by *Richter and Simmons* [1974], and thus coefficients of thermal expansion for materials on Mercury might differ from measurements in the literature. Moreover, fractured rock masses have lower bulk coefficients of thermal expansion than laboratory-scale samples.

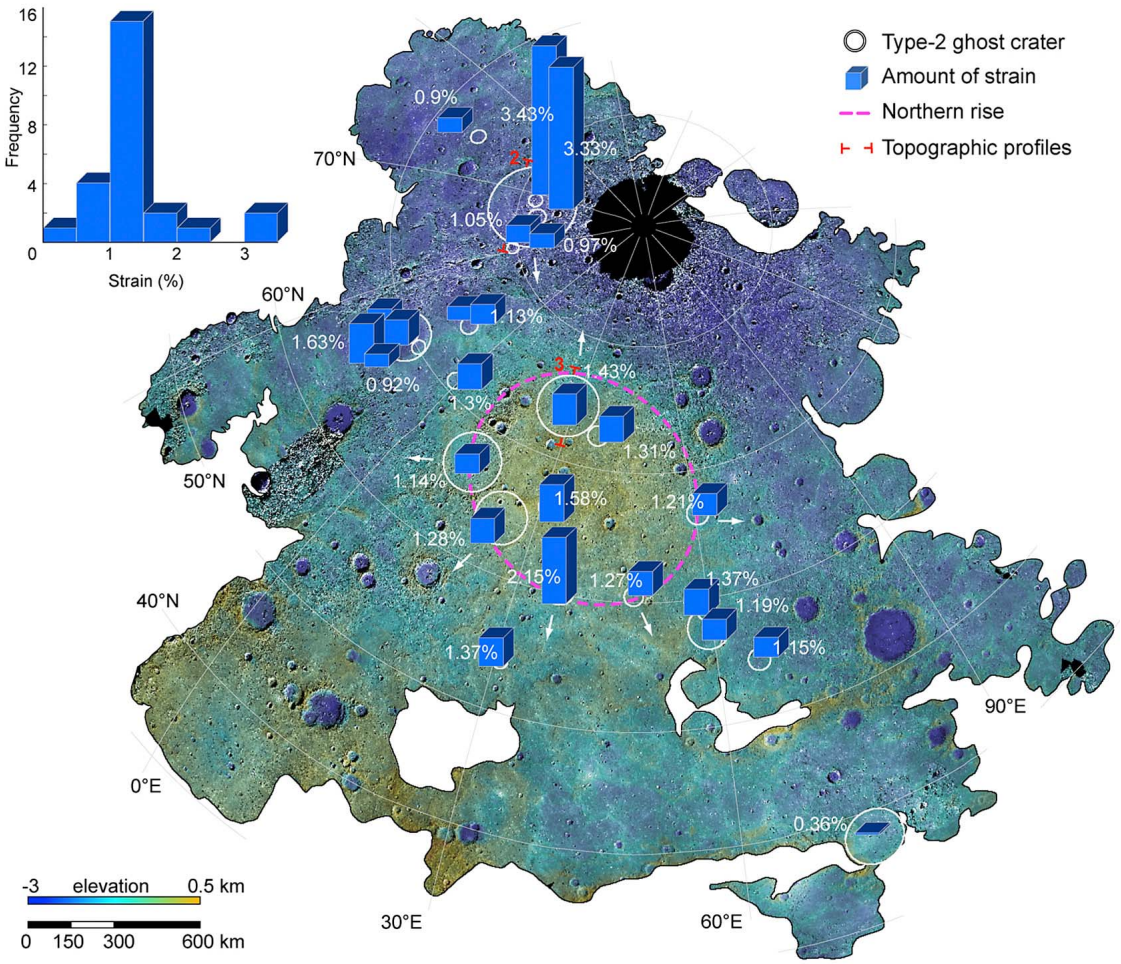

Figure 7. Calculated extensional longitudinal strain accommodated by graben within type-2 ghost craters in the northern smooth plains of Mercury, shown in polar stereographic projection on an MDIS monochrome base map overlaid by MLA topography [*Zuber et al.*, 2012]. A topographic rise (dashed green outline) is located in the center of the northern plains. The surfaces of type-2 ghost craters on the rise all tilt away from the area of highest rise topography (white arrows). Top left shows a histogram of longitudinal strain values. The majority are between 1 and 1.5%; strains greater than 3% are found within two ghost craters interior to the Goethe basin. The locations of the topographic profiles in Figures 2b and 3c are indicated in red.

[26] Nonetheless, under the assumption that the cooling units behaved as purely elastic, mechanically isotropic material, comparison of predicted strain values (Figure 8) with measured values for graben in type-2 ghost craters in Mercury's northern plains (Figure 7) shows that the majority of measured strains are within the range expected for thermal contraction. In addition, the lower number of graben found in the ghost craters of a given diameter in the plains units exterior to the Caloris basin indicates that strains there are lower, consistent with the expected lesser thermal contraction near Mercury's hot pole. However, the measured longitudinal strains for three type-2 ghost craters in the northern smooth plains exceed the expectation for thermal contraction, indicating either that strain values were higher than expected because of locally anomalous rock properties or that thermal contraction of these units may not have been the only mechanism responsible for graben formation in at least these examples of type-2 ghost craters.

[27] By the relationship given in equation (1), thermal contractional strain depends only on temperature change and rock physical properties and is independent of length scale, e.g., the diameter of the ghost crater or the thickness of the most recent lava flow units. However, the surficial extension should scale with the thickness of the layer in which the faults grew, leading to wider graben in thicker plains units and narrower graben in thinner units. Depending on individual unit thicknesses in layered rock sequences, faults can reach fracture saturation and form more or less homogeneously spaced fracture patterns [e.g., *Bai et al.*, 2000], with thicker layers generally marked by wider fracture spacing. *Cooke et al.* [2011] applied this expectation to models for the spacing of graben in the giant polygonal terrain of Utopia Planitia in which graben spacing, and hence polygon size, was greater for a thicker surficial layer. By this reasoning, the presence of a few wide graben in some, but not all, ghost craters on Mercury (Figure 1) is the result of a locally thick

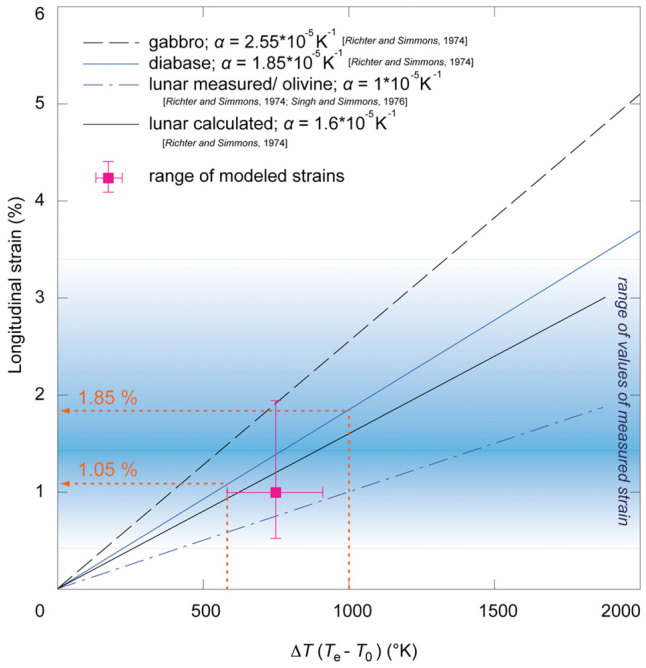

Figure 8. Predicted longitudinal strain as a function of temperature change for several rock types with measured or estimated coefficients of thermal expansion. *Richter and Simmons* [1974] determined coefficients either by experimental measurements on lunar samples and terrestrial diabases, compositionally equivalent to basalts, or by theoretical estimation from Turner's equation. Temperature changes between 600 and 1000 K for a rock of basaltic composition can cause up to 1 to 1.85% of longitudinal contraction after cooling below the elastic blocking temperature. Shaded in blue is the range of measured strain estimates, with an average at ∼1.3%. The strain predicted for the nominal thermal contraction model is indicated by the pink square; error bars denote the variations in predicted strain and total cooling among the models considered (see Figure 9).

cooling unit. In such a thicker unit, faults may have reached fracture saturation and were able to propagate to greater depths, accumulate more slip, and thus form wider graben. Thinner cooling units, such as those expected in the plains surrounding ghost craters, should have similar amounts of extensional strain, but in those areas the brittle deformation of thinner layers should result in smaller, more closely spaced fractures [e.g., *Bai et al.*, 2000].

3.2. Strain Modeling

[28] By means of the Abaqus thermomechanical finite element code employed by Freed et al. (submitted manuscript, 2012), we further explored models for thermal contractional strain within a volcanic unit that has buried an impact structure. In particular, we have investigated the effects on contractional strain of (1) the thickness of cooling unit, (2) the change in temperature, (3) the contrast in strength between the cooling unit and the underlying material, and (4) the horizontal scale (i.e., diameter) of the impact structure. To highlight the impact of these key parameters on modeled strains, we varied each parameter in isolation, keeping all other parameters constant. The nominal numerical model is in axisymmetric geometry for a 100-km-diameter crater with a 1 km thickness of fill. Fill thickness was taken to be constant within 30 km of the crater center and to thin smoothly to zero at the crater edge. Further parameters of the general model included a temperature change in the youngest cooling unit of $\Delta T = 900$ K and a ratio of the strength of the cooling unit to that of the underlying material of 10:1. The full description of the modeling procedure and parameters has been given by Freed et al. (submitted manuscript, 2012). If contraction caused by cooling of flood lavas was the major contributor to graben formation in type-2 ghost craters, then the sensitivity of calculated strain to variations in key parameters should provide insight into the thermomechanical evolution of volcanic plains more generally on Mercury.

[29] Results on the sensitivity of horizontal strains and stresses to variations in key parameters are presented in Figure 9. Thermal contraction results in extensional deformation because of the resistive forces imparted by the underlying, non-contracting material. Therefore, modeled negative strain values correspond to positive extensional stress values. Hence, predicted model strains (negative) and measured graben strains (positive) can be directly compared.

[30] In particular, horizontal strains increase with an increasing thickness of the cooling unit (Figure 9a), and thinner units experience higher horizontal thermal stresses. Horizontal strains between −1 and −2% result from cooling of a volcanic unit 1 to 2 km in thickness. For a fixed thickness of the cooling unit, strains are higher and stresses lower for smaller crater dimensions (Figure 9b). For a 1 km fill thickness, −1 to −2% of horizontal strain is seen for ghost craters having a radius between 30 and 50 km.

[31] Although longitudinal strains, as indicated by equation (1), are independent of length scale for linear traverses across the ghost craters, numerical simulations indicate that crater size and fill thickness can have a major influence on strains. This size dependence of strain is a consequence of the added dimension of depth. It is apparent from Figure 9 that keeping cooling unit thickness constant but decreasing crater diameter leads to higher horizontal strains. Likewise, keeping crater diameter constant and increasing cooling unit thickness increases the horizontal strain. Length-scale independence holds for crater geometries with the same ratio of cooling unit thickness to crater diameter, whereas increased thickness-to-diameter ratios produce higher horizontal strains and lower ratios produce lower strains.

[32] Simulations designed to explore the effect of different contrasts in strength between the cooling unit and the underlying material show that increasing the strength ratio leads to greater horizontal strains but lesser horizontal stresses. Strains within a cooling unit that is a factor of 20 stronger than its underlying substrate can be as high as ∼−2%, whereas low strength contrasts result in lower horizontal strains. Freed et al. (submitted manuscript, 2012) argued that a strength contrast between the materials is likely, given that the underlying rocks were weakened by impact crater formation before infilling by volcanic material.

[33] Simulations for different amounts of cooling below an elastic blocking temperature show that both final strain and final stress increase for increased cooling (Figure 9d). Changes in total cooling over the range of values likely on Mercury do not affect the horizontal strains as much as the variations in other model parameters considered here. For

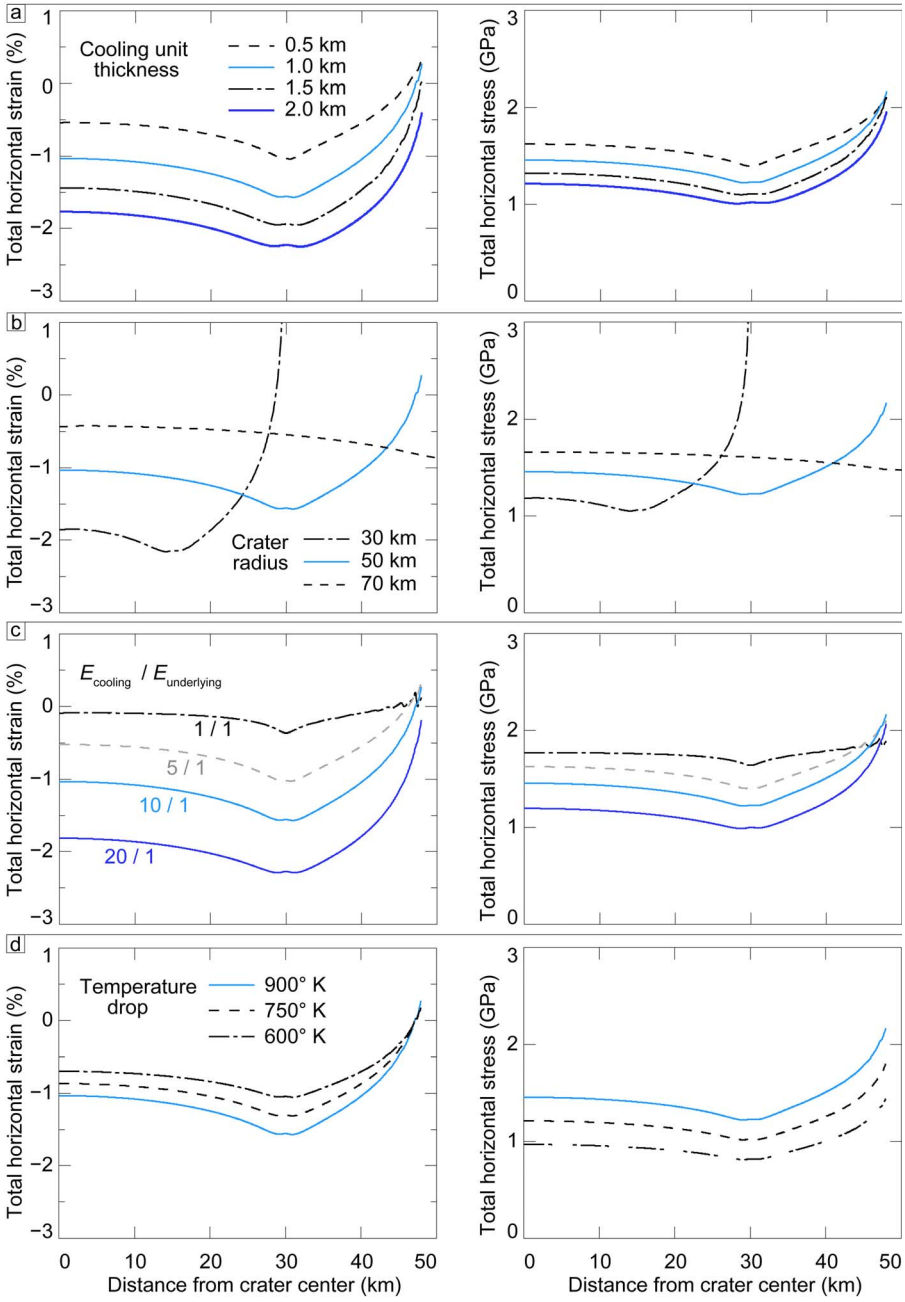

Figure 9. Effects of the cooling unit geometry and rock physical parameters on horizontal strains and stresses across a ghost crater from thermal contraction of volcanic fill, derived from finite element models similar to those described by Freed et al. (submitted manuscript, 2012). (a) Effects of cooling unit thickness. Thicker units show higher strains but lower stresses. (b) Effects of ghost crater radius. Smaller craters show higher strains but lower stresses. (c) Effects of the ratio of strength of the volcanic fill to that of the underlying material. Higher ratios produce higher strains and lower stresses. (d) Effects of total temperature change. Higher temperature changes produce higher strains and higher stresses.

example, a temperature drop of 600°C yields horizontal strains of −0.7%, only 0.3% different from the −1% of horizontal strain produced by a change in temperature of 900°C. The strain values are, in general, in accordance with those predicted from equation (1) (Figure 8) for a given temperature change. Differences between the simple predictions and the model simulations reflect the effects of basin geometry and the differing material properties of the cooling volcanic unit and the underlying rocks.

4. Implications for the Thermomechanical and Tectonic Evolution of Smooth Plains Units

[34] The style, distribution, and properties of faulting associated with volcanically buried ghost craters on Mercury have

implications for the geologic evolution of the smooth plains in which they are located. Fault displacements and depth extents of structures associated with ghost craters provide insight into the mechanical layering, and thus thicknesses, of the units in which they form. The depth extents of faulting for the graben can be estimated from their widths. Although *Schultz et al.* [2007] argued that, in many cases, graben widths cannot be directly correlated with layer thicknesses, they nonetheless found that graben widths do yield some information about the layers in which they are found.

[35] For type-2 ghost craters in Mercury's northern smooth plains, most graben have fairly uniform widths of ~1 km, a value that is fairly constant along the lengths of individual graben, suggesting constant depths of faulting and possibly vertical restriction of the faults [e.g., *Nicol et al.*, 1996; *Polit et al.*, 2009]. These observations imply that these graben grew in a single mechanical unit, the thickness of which can be approximated by the depth extent of the graben-bounding faults. Given the hourglass model for graben formation and a fault dip angle of 60°, consistent with the optimum orientation of the frictional slip plane for normal faults in basaltic rock [*Jaeger et al.*, 2007], the depth extent of faulting may be estimated to have been ~1.5 to 2 km for most of the graben in type-2 ghost craters. In comparison, depth extents of faulting inferred with an idealized symmetric graben geometry [*Melosh and Williams*, 1989] give a lower limit, so that graben that are ~1 km wide would have a minimum depth extent of ~1 km. The increased graben widths in the two ghost craters within Goethe basin suggest that the layer in which those graben formed is thicker. Moreover, those graben do not display constant widths along their lengths, indicating unrestricted fault growth.

[36] From these depth extents of faulting, we conclude that there was substantial pooling of the youngest major episode of flood lava emplacement in ghost craters. The uppermost unit of volcanic infill in the majority of type-2 ghost craters must have been at least 1 km thick in order to have developed the graben geometries observed from thermal contraction alone.

[37] Correlating the thickness of volcanic fill to the morphology of the host craters and basins leads to further inferences about the subsurface geologic conditions in smooth plains areas. Original crater depths can be inferred from laser altimeter profiles of similarly sized fresh craters [*Barnouin et al.*, 2012] or by the use of crater scaling laws [*Pike*, 1977, 1988]. Because all type-2 ghost craters have diameters in excess of 40 km, the original crater depths must have been greater than 3 km. This result implies that the uppermost volcanic material overlies one or more earlier flooding units, and that the largest expanses of volcanic plains on Mercury were emplaced in several flooding events. The earliest flood lavas likely pooled within earlier-formed impact craters and basins and solidified and cooled before the most recent major plains unit was emplaced. The top of the earlier plains material would have formed a thermal and mechanical boundary beneath the cooling unit in which the latest graben population grew.

[38] Multiple episodes of flood volcanism and pooling of plains lavas are consistent with the findings from the sensitivity analysis of finite element models for thermal contractional strain (Figure 9). Measured longitudinal strains of $\varepsilon_l \sim$ 1.5% (Figure 7) compare best to modeled strains for flooded basins 100 km in diameter for a youngest cooling unit that is about 1.5 km thick (Figure 9a), and higher strains are predicted for smaller ghost craters (Figure 9b). Because the effects of uncertainties in the total cooling are small (Figure 9d), and parameters governing rock strength and thermal expansion coefficients are unlikely to differ substantially among plains units, variations in measured longitudinal strains across ghost craters are likely to reflect primarily different combinations of the thickness of the uppermost volcanic unit and the geometry of the underlying crater.

[39] Because type-2 ghost craters do not appear to be spatially restricted (Figure 1), variations in the thickness of the uppermost cooling unit is also regarded as a primary contributor to the lack of graben in some ghost craters [*Watters et al.*, 2012; Freed et al., submitted manuscript, 2012]. By this view, the surficial volcanic unit in type-1 ghost craters may have been too thin for a prominent graben pattern to develop. Likewise, the wider graben responsible for the anomalously high values of measured longitudinal strain of $\varepsilon_l > 3\%$ in smaller type-2 ghost craters suggest greater thicknesses of the youngest fill unit in these structures. Moreover, as shown by the numerical models, a smaller crater will experience greater thermal contractional strains for a given thickness of the youngest volcanic unit (Figure 9b).

[40] As mentioned above, other mechanisms might have contributed to strains in areas where measured strains are highest (i.e., $\varepsilon_l > 3\%$). Indeed, as noted in section 3.1, the floors of ghost craters (Figures 2 and 3) tilt away from the peak of a broad topographic rise within the northern smooth plains (Figure 7) [*Zuber et al.*, 2012; *Solomon et al.*, 2012]. The formation of the rise must have postdated the emplacement of the northern smooth plains, in part because the even distribution and similar widths of graben within each of the ghost craters around the rise require fairly constant plains thicknesses of the trough-bearing units in these ghost craters. In contrast, the floors of many fresh craters superposed on the northern rise and up to ~80 km in diameter do not show systematic tilts that correlate with rise topography [*Solomon et al.*, 2012], showing that processes responsible for the topographic change had largely ceased by the time of these impacts.

[41] Ghost craters of all types appear confined to the smooth plains. Figure 1 shows the currently mapped distribution of smooth plains in which ghost craters are found in Mercury's northern hemisphere. The majority of ghost craters occur in the central portions of plains units, and many appear to form a linear trend from northeast to southwest across the northern hemisphere. A few ghost craters are seen near the edges of the smooth plains. These features, as well as most of the type-2 ghost craters in the Caloris exterior plains (Figure 5), have portions of their crater rims exposed and contain graben narrower than those observed in the northern smooth plains. Together, these observations indicate a lesser thickness of youngest plains material at the edges of plains and a generally thinner upper volcanic unit in the Caloris exterior plains. A comparison of mapped locations of volcanic smooth plains with a map of northern hemisphere crustal thickness derived from topography and gravity [*Smith et al.*, 2012] shows that the centers of these plains, and therefore most of the ghost craters they host, coincide with areas of thinner than average crust. This comparison may indicate nothing more than that most long-

wavelength variations in elevation are isostatically compensated by offsetting variations in crustal thickness and that smooth plains deposits are preferentially located in areas of low elevation. Nonetheless, further analyses of topography, crustal thickness, plains emplacement, and deformation should illuminate this and other spatial relationships and allow for more detailed interpretations of the locations and origins of flood volcanic provinces on Mercury.

5. Conclusions

[42] Volcanic smooth plains on Mercury contain populations of several types of ghost craters, characterized by partial or complete wrinkle-ridge rings or graben rings, and often by wrinkle-ridge rings that enclose an area deformed by graben. The presence of graben in ghost craters allows for the quantification and assessment of strains across the craters. Moreover, comparisons with simple predictions and finite element models provide tests of the proposal that graben formation in this class of features was the result of thermal contraction of the volcanic fill [*Head et al.*, 2011; *Watters et al.*, 2012; Freed et al., submitted manuscript, 2012]. The strain analysis and modeling, together with the application of knowledge of graben geometries and graben development mechanisms to high-resolution images of the graben in ghost craters, provide clues to the thicknesses and physical properties of major geological units and more generally improve our understanding of plains evolution and emplacement. In particular, we find that the volcanic units in which the graben developed must be at least 1.5 km thick to accommodate observed graben geometries. Such a thickness is not sufficiently great to have fully filled in a single event the impact structures now preserved as ghost craters, suggesting that infilling occurred in several stages and that the thickest portions of the youngest flood lava cooling units are those most likely to have experienced the deformation recorded by graben seen within ghost craters today.

[43] **Acknowledgments.** We thank Michelle Cooke and Chris Okubo for helpful comments on an earlier draft. The MESSENGER project is supported by the NASA Discovery Program under contracts NASW-00002 to the Carnegie Institution of Washington and NAS5-97271 to the Johns Hopkins University Applied Physics Laboratory.

References

Bai, T., D. D. Pollard, and H. Hao (2000), Explanation for fracture spacing in layered materials, *Nature*, *403*, 753–756, doi:10.1038/35001550.

Barnouin, O. S., M. T. Zuber, D. E. Smith, G. A. Neumann, R. R. Herrick, J. E. Chappelow, S. L. Murchie, and L. M. Prockter (2012), The morphology of craters on Mercury: Results from MESSENGER flybys, *Icarus*, *219*, 414–427, doi:10.1016/j.icarus.2012.02.029.

Buczkowski, D. L., and M. L. Cooke (2004), Formation of double-ring circular graben due to volumetric compaction over buried impact craters: Implications for thickness and nature of cover material in Utopia Planitia, Mars, *J. Geophys. Res.*, *109*, E02006, doi:10.1029/2003JE002144.

Buczkowski, D. L., H. V. Frey, J. H. Roark, and G. E. McGill (2005), Buried impact craters: A topographic analysis of quasi-circular depressions, Utopia Basin, Mars, *J. Geophys. Res.*, *110*, E03007, doi:10.1029/2004JE002324.

Cavanaugh, J. F., J. C. Smith, X. Sun, A. E. Bartels, L. Ramos-Izquierdo, D. J. Krebs, J. F. McGarry, R. Trunzo, A. M. Novo-Gradac, and J. L. Britt (2007), The Mercury Laser Altimeter instrument for the MESSENGER mission, *Space Sci. Rev.*, *131*, 451–479, doi:10.1007/s11214-007-9273-4.

Cooke, M., F. Islam, and G. McGill (2011), Basement controls on the scale of giant polygons in Utopia Planitia, Mars, *J. Geophys. Res.*, *116*, E09003, doi:10.1029/2011JE003812.

Cruikshank, D. P., W. K. Hartmann, and C. A. Wood (1973), Moon: 'Ghost' craters formed during mare filling, *Moon*, *7*, 440–452, doi:10.1007/BF00564645.

Fassett, C. I., J. W. Head, D. T. Blewett, C. R. Chapman, J. L. Dickson, S. L. Murchie, S. C. Solomon, and T. R. Watters (2009), Caloris impact basin: Exterior geomorphology, stratigraphy, morphometry, radial sculpture, and smooth plains deposits, *Earth Planet. Sci. Lett.*, *285*, 297–308, doi:10.1016/j.epsl.2009.05.022.

Frey, H. V., J. H. Roark, K. M. Shockey, E. L. Frey, and S. E. H. Sakimoto (2002), Ancient lowlands on Mars, *Geophys. Res. Lett.*, *29*(10), 1384, doi:10.1029/2001GL013832.

Hartmann, W. K., and G. Esquerdo (1999), "Pathological" Martian craters: Evidence for a transient obliteration event?, *Meteorit. Planet. Sci.*, *34*, 159–165, doi:10.1111/j.1945-5100.1999.tb01742.x.

Hawkins, S. E., III, et al. (2007), The Mercury Dual Imaging System on the MESSENGER spacecraft, *Space Sci. Rev.*, *131*, 247–338, doi:10.1007/s11214-007-9266-3.

Head, J. W., et al. (2008), Volcanism on Mercury: Evidence from the first MESSENGER flyby, *Science*, *321*, 69–72, doi:10.1126/science.1159256.

Head, J. W., et al. (2009), Volcanism on Mercury: Evidence from the first MESSENGER flyby for extrusive and explosive activity and the volcanic origin of plains, *Earth Planet. Sci. Lett.*, *285*, 227–242, doi:10.1016/j.epsl.2009.03.007.

Head, J. W., et al. (2011), Flood volcanism in the northern high latitudes of Mercury revealed by MESSENGER, *Science*, *333*, 1853–1856, doi:10.1126/science.1211997.

Jaeger, J. C., N. G. W. Cook, and R. W. Zimmerman (2007), *Fundamentals of Rock Mechanics*, 4th ed., 593 pp., Blackwell, Oxford, U. K.

Klimczak, C., R. A. Schultz, and A. L. Nahm (2010), Evaluation of the origin hypotheses of Pantheon Fossae, central Caloris basin, Mercury, *Icarus*, *209*, 262–270, doi:10.1016/j.icarus.2010.04.014.

Mangold, N. (2005), High latitude patterned grounds on Mars: Classification, distribution and climatic control, *Icarus*, *174*, 336–359, doi:10.1016/j.icarus.2004.07.030.

Melosh, H. J., and W. B. McKinnon (1988), The tectonics of Mercury, in *Mercury*, edited by F. Vilas, C. R. Chapman, and M. S. Matthews, pp. 374–400, Univ. of Ariz. Press, Tucson.

Melosh, H. J., and C. A. Williams Jr. (1989), Mechanics of graben formation in crustal rocks: A finite element analysis, *J. Geophys. Res.*, *94*, 13,961–13,973, doi:10.1029/JB094iB10p13961.

Murchie, S. L., et al. (2008), Geology of the Caloris basin, Mercury: A view from MESSENGER, *Science*, *321*, 73–76, doi:10.1126/science.1159261.

Nicol, A., J. Watterson, J. J. Walsh, and C. Childs (1996), The shapes, major axis orientations and displacement patterns of fault surfaces, *J. Struct. Geol.*, *18*, 235–248, doi:10.1016/S0191-8141(96)80047-2.

Nittler, L. R., et al. (2011), The major-element composition of Mercury's surface from MESSENGER X-ray spectrometry, *Science*, *333*, 1847–1850, doi:10.1126/science.1211567.

Pike, R. J. (1977), Size-dependence in the shape of fresh impact craters on the Moon, in *Impact and Explosion Cratering*, edited by D. J. Roddy, R. O. Pepin, and R. B. Merrill, pp. 489–509, Pergamon Press, New York.

Pike, R. J. (1988), Geomorphology of impact craters on Mercury, in *Mercury*, edited by F. Vilas, C. R. Chapman, and M. S. Matthews, pp. 165–273, Univ. of Ariz. Press, Tucson.

Polit, A. T., R. A. Schultz, and R. Soliva (2009), Geometry, displacement-length scaling, and strain of normal faults on Mars with inferences on mechanical stratigraphy of the Martian crust, *J. Struct. Geol.*, *31*, 662–673, doi:10.1016/j.jsg.2009.03.016.

Prockter, L. M., et al. (2010), Evidence for young volcanism on Mercury from the third MESSENGER flyby, *Science*, *329*, 668–671, doi:10.1126/science.1188186.

Richter, D., and G. Simmons (1974), Thermal expansion behavior of igneous rocks, *Int. J. Rock Mech. Min. Sci.*, *11*, 403–411, doi:10.1016/0148-9062(74)91111-5.

Schultz, P. H. (1976), Floor-fractured lunar craters, *Moon*, *15*, 241–273, doi:10.1007/BF00562240.

Schultz, R. A., J. M. Moore, E. B. Grosfils, K. L. Tanaka, and D. Mége (2007), The Canyonlands model for planetary grabens: Revised physical basis and implications, in *The Geology of Mars: Evidence from Earth-Based Analogs*, edited by M. Chapman, pp. 371–399, Cambridge Univ. Press, Cambridge, U. K., doi:10.1017/CBO9780511536014.016.

Singh, H. P., and G. Simmons (1976), X-ray determination of thermal expansion of olivines, *Acta Crystallogr., Sect. A Cryst. Phys. Diffr. Theor. Gen. Crystallogr.*, *32*, 771–773, doi:10.1107/S0567739476001575.

Smith, D. E., et al. (2012), Gravity field and internal structure of Mercury from MESSENGER, *Science*, *336*, 214–217, doi:10.1126/science.1218809.

Smrekar, S. E., P. Moreels, and B. J. Franklin (2002), Characterization and formation of polygonal fractures on Venus, *J. Geophys. Res.*, *107*(E11), 5098, doi:10.1029/2001JE001808.

Soliva, R., and A. Benedicto (2005), Geometry, scaling relations and spacing of vertically restricted normal faults, *J. Struct. Geol.*, *27*, 317–325, doi:10.1016/j.jsg.2004.08.010.

Soliva, R., A. Benedicto, and L. Maerten (2006), Spacing and linkage of confined normal faults: Importance of mechanical thickness, *J. Geophys. Res.*, *111*, B01402, doi:10.1029/2004JB003507.

Solomon, S. C. (1977), The relationship between crustal tectonics and internal evolution in the Moon and Mercury, *Phys. Earth Planet. Inter.*, *15*, 135–145, doi:10.1016/0031-9201(77)90026-7.

Solomon, S. C., et al. (2008), Return to Mercury: A global perspective on MESSENGER's first Mercury flyby, *Science*, *321*, 59–62, doi:10.1126/science.1159706.

Solomon, S. C., et al. (2012), Long-wavelength topographic change on Mercury: Evidence and mechanisms, *Lunar Planet. Sci.*, *XLIII*, Abstract 1578.

Spudis, P. D., and J. E. Guest (1988), Stratigraphy and geologic history of Mercury, in *Mercury*, edited by F. Vilas, C. R. Chapman, and M. S. Matthews, pp. 374–400, Univ. of Ariz. Press, Tucson.

Strom, R. G. (1971), Lunar mare ridges, rings and volcanic ring complexes, *Mod. Geol.*, *2*, 133–157.

Strom, R. G., N. J. Trask, and J. E. Guest (1975), Tectonism and volcanism on Mercury, *J. Geophys. Res.*, *80*, 2478–2507, doi:10.1029/JB080i017p02478.

Turcotte, D. L. (1983), Thermal stresses in planetary elastic lithospheres, *J. Geophys. Res.*, *88*, 585–587, doi:10.1029/JB088iS02p0A585.

Vasavada, A. R., D. A. Paige, and S. E. Wood (1999), Near-surface temperatures on Mercury and the Moon and the stability of polar ice deposits, *Icarus*, *141*, 179–193, doi:10.1006/icar.1999.6175.

Watters, T. R. (1993), Compressional tectonism on Mars, *J. Geophys. Res.*, *98*, 17,049–17,060, doi:10.1029/93JE01138.

Watters, T. R., S. L. Murchie, M. S. Robinson, S. C. Solomon, B. W. Denevi, S. L. André, and J. W. Head (2009a), Emplacement and tectonic deformation of smooth plains in the Caloris basin, Mercury, *Earth Planet. Sci. Lett.*, *285*, 309–319, doi:10.1016/j.epsl.2009.03.040.

Watters, T. R., J. W. Head, S. C. Solomon, M. S. Robinson, C. R. Chapman, B. W. Denevi, C. I. Fassett, S. L. Murchie, and R. G. Strom (2009b), Evolution of the Rembrandt impact basin on Mercury, *Science*, *324*, 618–621, doi:10.1126/science.1172109.

Watters, T. R., S. C. Solomon, M. S. Robinson, J. W. Head, S. L. André, S. A. Hauck II, and S. M. Murchie (2009c), The tectonics of Mercury: The view after MESSENGER's first flyby, *Earth Planet. Sci. Lett.*, *285*, 283–296, doi:10.1016/j.epsl.2009.01.025.

Watters, T. R., S. C. Solomon, C. Klimczak, A. M. Freed, J. W. Head, C. M. Ernst, D. M. Blair, T. A. Goudge, and P. K. Byrne (2012), Extension and contraction within volcanically buried impact craters and basins on Mercury, *Geology*, doi:10.1130/G33725.1, in press.

Weider, S. Z., L. R. Nittler, R. D. Starr, P. K. Byrne, D. K. Hamara, T. J. McCoy, and S. C. Solomon (2012), Compositional heterogeneity on Mercury's surface revealed by MESSENGER's X-Ray Spectrometer, *Lunar Planet. Sci.*, *XLIII*, Abstract 1472.

Williams, J.-P., J. Ruiz, M. A. Rosenburg, O. Aharonson, and R. J. Phillips (2011), Insolation driven variations of Mercury's lithospheric strength, *J. Geophys. Res.*, *116*, E01008, doi:10.1029/2010JE003655.

Zuber, M. T., et al. (2012), Topography of the northern hemisphere of Mercury from MESSENGER laser altimetry, *Science*, *336*, 217–220, doi:10.1126/science.1218805.